Ultrafast Pulsed Laser Annealing of $Pd_{100-x}Si_x$ Thin Films

O. Liubchenko[a,*], I. Jacyna[a], T.J. Albert[b], J. Antonowicz[c],
M. Chojnacki[a], A.-C. Dippel[d], P. Dzięgielewski[c], O. Gutowski[d],
D. Klinger[a], Z. Kostera[c], R. Minikayev[a], K. Sokolowski-Tinten[b],
W. Zajkowska-Pietrzak[a] and R. Sobierajski[a]

[a]*Institute of Physics Polish Academy of Sciences, al. Lotników 32/46, 02-668 Warsaw, Poland*
[b]*Faculty of Physics and Center for Nanointegration Duisburg-Essen (CENIDE), University of Duisburg-Essen, Lotharstrasse 1, 47048 Duisburg, Germany*
[c]*Faculty of Physics, Warsaw University of Technology, Koszykowa 75, 00-662 Warsaw, Poland*
[d]*Deutsches Elektronen Synchrotron DESY, Notkestraße 85, 22607 Hamburg, Germany*

Excitation of materials by ultrashort laser pulses is characterized initially by a strong non-equilibrium between the electronic and lattice degrees of freedom. This is followed by a rapid transfer of the electronic excess energy to the lattice, which leads to heating within a few picoseconds. In thin films deposited on a substrate, the subsequent nanosecond-scale quenching is driven by rapid heat diffusion into the substrate. This non-equilibrium heating–cooling cycle with ultrahigh heating and cooling rates enables access to metastable states that are difficult to reach with conventional techniques. In this work, we report on a comprehensive characterization of structural changes driven by ultrashort pulsed laser annealing in thin $Pd_{100-x}Si_x$ films ($x = 0, 3, 5, 10, 17\%$). The combined use of microscopy and X-ray diffraction for post-mortem analysis provides new insights into the composition-dependent crystallization behavior. By analyzing optical images from a series of laser irradiations at varying pulse energies (fluence scan), a two-dimensional fluence map was reconstructed for an arbitrary pulse energy. This enabled a direct correlation between deposited energy density, surface morphology, and structural changes derived from the micro-X-ray diffraction measurements analyzed using the Rietveld method. Above a fluence threshold of 25 mJ/cm^2, all samples exhibit significant structural modifications — changes of the surface morphology, an increase of the lattice parameters, reduction of strain, grain growth, and reduced amorphous contributions. These observations are consistent with a scenario in which the sample undergoes ultrafast melting, followed by rapid cooling and recrystallization, thereby relaxing towards a lower energy state. Notably, only the face-centered cubic phase of crystalline Pd was observed across all samples and irradiation conditions, in contrast to the equilibrium phase diagram including the Pd–Si compounds. This confirms that ultrafast laser treatment produces metastable states, previously unreported in Pd–Si alloys.

topics: Pd–Si alloys, X-ray diffraction (XRD), ultrashort pulsed laser annealing

1. Introduction

Multicomponent Pd-based alloys are known for their exceptional glass-forming ability (GFA), which enables them to be cast in bulk form [1–3]. Among these systems, Pd–Si binary alloys have been shown to form bulk metallic glasses near a deep eutectic composition of around 19 at.% Si [4–6]. The high stability of eutectic Pd–Si liquids facilitates vitrification at remarkably low cooling rates, on the order of only a few K/s [7]. In contrast, pure Pd exhibits virtually no GFA and, similar to other face-centered cubic (fcc) metals, crystallizes even

under ultrafast quenching conditions approaching 10^{14} K/s [8]. To date, glassy Pd has been observed exclusively in computer simulations [9]. This pronounced compositional dependence on GFA reflects significant changes in the nucleation kinetics and crystal growth with increasing Si content [10].

In this respect, short pulse laser annealing offers unique opportunities since it enables quenching rates approaching 10^{12} K/s [11–13]. Surprisingly, this approach has so far not really been used for Pd–Si alloys. We are aware of only one study in which annealing with picosecond pulses (20–200 ps) has been investigated as an intermediate processing step in the crystallization of near-eutectic

Density, thickness, and roughness of the as-grown $Pd_{100-x}Si_x$ films.

Sample	Parameters of the $Pd_{100-x}Si_x$ film			Parameters of the SiN cap		
	Density [g/cm^3]	Thickness [nm]	Roughness [nm]	Density [g/cm^3]	Thickness [nm]	Roughness [nm]
$Pd_{100}Si_0$	13.6	19.2	0.94	2.9	4.8	0.99
$Pd_{97}Si_3$	13.7	19.0	0.47	2.9	4.7	0.52
$Pd_{95}Si_5$	13.6	18.8	0.39	2.9	4.8	0.41
$Pd_{90}Si_{10}$	13.1	22.0	0.39	2.9	5.2	0.50
$Pd_{83}Si_{17}$	12.5	23.6	0.38	2.9	4.9	0.52

Pd–Si amorphous alloys with relatively long (~ 1 s) laser pulses [14]. While it was found that picosecond laser-treated glasses exhibit superior stability against devitrification compared to the as-quenched glasses, no direct structural characterization of picosecond laser-annealed Pd–Si alloys was reported.

In this work, we characterize the structural changes of thin (20 nm) $Pd_{100-x}Si_x$ alloys with varying Si content ($x = 0, 3, 5, 10, 17$ at. %) in a yet unexplored heating and cooling regime using femtosecond laser excitation. A key characteristic of the temperature evolution following such excitation of thin films with thickness comparable to the optical absorption depth (10–20 nm in metals) is the spatially localized, quasi-1D nature of the temperature evolution. On the one hand, this allows uniform in-depth heating of the film at extreme heating rates (up 10^{15} K/s) due to the strong electron–phonon coupling [15]. On the other hand, the subsequent thermal response is dominated by heat conduction across the interface into the substrate at quenching rates of 10^{11}–10^{12} K/s, while lateral transport is negligible due to weak lateral temperature gradients at typical laser spot sizes of about 100 μm. Therefore, the evolution at each position in the irradiated sample area represents, to a very good approximation, the response to the given local value of excitation fluence. This, in combination with the uniform in-depth heating mentioned above, constrains the energy distribution to an effectively two-dimensional (2D) spatial profile.

Using a micro-focused synchrotron X-ray beam, we mapped the laser-irradiated spot and acquired X-ray diffraction (XRD) patterns in transmission geometry. Rietveld refinement of these patterns allowed us to quantify key structural parameters of the films (lattice parameter, microstrain, crystalline grain size, and amorphous/crystalline fraction) as a function of the laser pulse fluence. Our results demonstrate how film composition influences microstructure development at different laser fluences, and we conclude on the role of the Si content in governing the structural evolution during pulsed laser annealing.

2. Materials and methods

We have investigated ~ 20 nm thick $Pd_{100-x}Si_x$ films deposited by magnetron sputtering on 50-nm-thick SiN membranes supported by a silicon frame (produced by Silson Ltd [16]). A 5-nm-thick silicon nitride cap, prepared by reactive magnetron sputtering, was used to prevent sample's contamination by atmospheric gases[†]. Figure 1a shows a schematic layout of the sample.

As-grown reference samples ($Pd_{100-x}Si_x$ films with a SiN cap deposited on a bulk Si substrate) were pre-characterized using laboratory X-ray reflectometry (XRR) with a Philips X'Pert MPD diffractometer to determine the thickness, density, and roughness of the $Pd_{100-x}Si_x$ films and SiN caps (results are presented in Table I).

Structural and surface morphology modifications of the films were induced using ultrashort (0.25 ps) laser pulses with a wavelength of 515 nm. The optical beam was focused on the sample at normal incidence to a spot with a full width at half maximum (FWHM) of ≈ 210 μm. The samples were irradiated in single-shot mode (i.e., one laser shot per one window — see Fig. 1) with pulse energies ranging from 8.7 to 49 μJ, corresponding to peak densities of an incident energy per area (fluences) of 17 to 98 mJ/cm^2.

[†1] Deposition was carried out in a high-vacuum chamber with a base pressure of 10^{-9} mbar, equipped with multiple two-inch magnetrons for co-sputtering. The substrates were preheated to slightly above 100°C for 5 h to remove residual atmospheric gases before being cooled to room temperature for film deposition. High-purity palladium (99.999%) and N-type silicon (99.999%) targets served as the source materials for sputtering the metallic and cap films. The sputtering process of the $Pd_{100-x}Si_x$ film was conducted in an argon (99.999%) atmosphere at a pressure of 7×10^{-3} mbar using direct current (DC) power supplies. After deposition, the films were coated with a 5 nm thick SiN cap via reactive sputtering in the same chamber in an N_2-Ar gas mixture atmosphere with a volumetric ratio N_2 : Ar = 1.15 : 1. The chamber pressure remained at 7×10^{-3} mbar during the process, and sputtering was performed using a DC power supply with a 120 kHz pulse function.
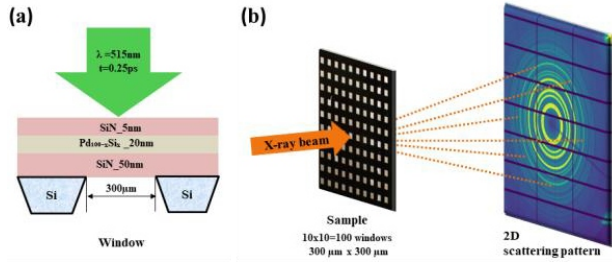
Fig. 1. (a) Schematic layout of the sample and (b) geometry of the X-ray diffraction experiment. More details are given in the text.

The post-irradiation analysis of the exposed spots was performed using Nomarski DIC (differential interference contrast) optical microscopy with a Zeiss Axio Scope A1 microscope and by scanning electron microscopy using a SEM/FIB HELIOS 600 scanning electron microscope (SEM).

Subsequently, a micro-XRD structural analysis was performed on both as-grown and laser-irradiated samples. For the laser-irradiated samples, the analysis was conducted on selected single-pulse laser-irradiated spots with fluences of 70, 65, 60, 70, and 60 mJ/cm^2 for samples with Si contents of 0%, 3%, 5%, 10%, and 17%, respectively. The local atomic structure was characterized by means of X-ray diffraction in transmission geometry with a micro-focused 73.47 keV X-ray beam (2 μm × 20 μm FWHM, i.e, respectively, vertical × horizontal) at beamline P07 of the PETRA III synchrotron [17]. The micro-XRD measurements of the as-grown samples were performed near the center of the non-irradiated window. To characterize the irradiated spots, a series of micro-XRD measurements were conducted across the irradiated area, with approximately 20 μm spacing between each measurement (see Fig. 3c — black horizontal lines). To minimize background scattering of X-rays in air, measurements were conducted in a vacuum chamber. The diffraction patterns were recorded using a PILATUS CdTe 2M flat-panel detector. A schematic of the diffraction setup used in the experiment is shown in Fig. 1b.

3. Results

3.1. Surface morphology and fluence profile in the laser spot

The microscopy images in Fig. 2 show the laser-irradiated spots for a peak fluence of 70 mJ/cm^2, which reveal changes in surface morphology for all types of investigated samples. These changes are qualitatively similar for samples with a Si content varying from 0 to 10%. However, the microscopy image of the $Pd_{83}Si_{17}$ sample appears noticeably different, which we attribute to the higher Si content

$Pd_{100}Si_0$ $Pd_{97}Si_{03}$
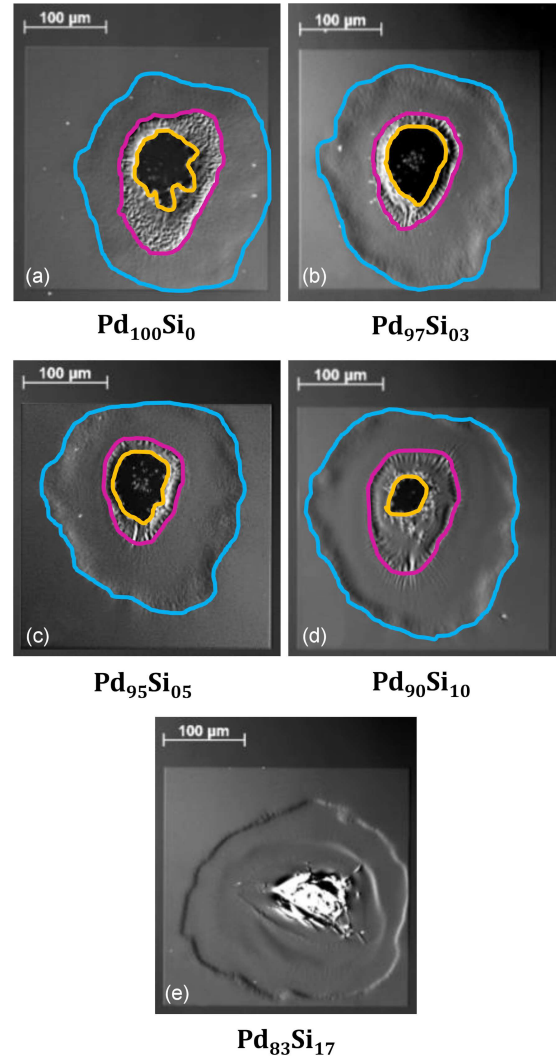
$Pd_{95}Si_{05}$ $Pd_{90}Si_{10}$

$Pd_{83}Si_{17}$

Fig. 2. Microscopy images of the surface morphology of the investigated samples after exposure to a single laser pulse of a fluence 70 mJ/cm^2. Visible changed regions are highlighted.

and its the near-eutectic composition. This observation is in line with the results of the structural characterization, as discussed further below.

For $x = 0$–10%, distinct regions with clearly defined boundaries can be identified, indicating threshold behavior, i.e., that the formation of a particular feature occurs only when the corresponding threshold fluence is locally reached/exceeded. At the periphery of the irradiated area, corresponding to low irradiation fluences, no visible changes are observed. As the laser fluence increases towards the center, a ring of surface wrinkles emerges (blue contour in Fig. 2) — for clarity, hereinafter named as the "outer wrinkles ring". It smoothly (without a distinct threshold) transitions into a region where the surface again appears flat (similar to the non-affected area). At an even higher local fluence (purple contour in Fig. 2), a threshold transition, resembling a rim, becomes visible. Inside the

purple contour, the surface again exhibits a wrinkled appearance (henceforth referred to as the "inner wrinkles ring"). At the very center of the spots corresponding to the fluences close to the peak fluence (yellow contour in Fig. 2), material removal is evident. In contrast, the surface modifications of the $Pd_{83}Si_{17}$ sample (Fig. 2e) are clearly different than the ones observed at lower Si-content. Note that (i) the wrinkling is much less pronounced and limited to the corresponding threshold region; (ii) the center region does not show clear indications of material removal. As will be discussed further below, the structural modifications of this sample are also significantly different compared to the other samples.

The fluence dependence on the observed morphological changes has been analyzed for each sample separately. The fluence scan method [18] was applied. For each spot generated at a given laser pulse energy E, a contour corresponding to the boundaries of a chosen region (as classified above) and thus the corresponding threshold fluence was drawn, and the enclosed area S was measured. The enclosed area S was plotted as a function of $\ln(E)$ and analyzed following the method described by Liu [19], which provides the threshold energies E_{th} for each type of morphological change. This approach was applied to all investigated $Pd_{100-x}Si_x$ sample compositions, with x values of 0, 3, 5, 10, and 17 at.%. Next, the relation E_{th}/E vs S was plotted and fitted with an exponential function $E_{th}/E = A\exp(-S/S_0)$, where A is the correction factor for the threshold energy and S_0 is the so-called effective area of the laser beam. The threshold fluence for each type of morphological change on a given sample was then calculated as $F_{th} = A\,E_{th}/S_0$ [18]. To test the hypothesis that the morphological changes depend on the local laser fluence threshold, the data points F_{th}/F vs S for a given sample region were plotted in the same figure (see Fig. 3a). The experimental data clearly follow the same exponential curve. This validates the used approach. Furthermore, one can conclude that the processes leading to the formation of particular structural changes depend only on the local deposited energy density and are indeed unaffected by lateral effects such as in-plane heat diffusion (described in Sect. 1).

The summarized values of the threshold energies E_{th} and fluences F_{th} (grouped in sets of three, corresponding to the blue, purple and yellow contours in Fig. 2, respectively), are shown in Table II. The calculated laser beam effective area S_0 is the same for all cases and equal to approximately $50000\ \mu m^2$.

Next, all contours obtained for a given sample type were superimposed on a single figure. Each contour corresponds to a specific area S and normalized fluence F_{th}/F_0, where F_{th} is the threshold associated with the contour, and F_0 is the maximum fluence at the location where the contour

TABLE II

The experimentally established threshold energies E_{th} and the fluences F_{th} for all types of samples. See details in the text.

Sample	E_{th} [μJ]	F_{th} [mJ/cm^2]
$Pd_{100}Si_0$	$12 \pm 5\%$	$25 \pm 6\%$
	$24 \pm 3\%$	$51 \pm 4\%$
	$32 \pm 2\%$	$67 \pm 3\%$
$Pd_{97}Si_{03}$	$11 \pm 8\%$	$25 \pm 10\%$
	$27 \pm 3\%$	$60 \pm 4\%$
	$31 \pm 2\%$	$69 \pm 3\%$
$Pd_{95}Si_{05}$	$11 \pm 7\%$	$24 \pm 8\%$
	$29 \pm 2\%$	$62 \pm 3\%$
	$33 \pm 2\%$	$71 \pm 3\%$
$Pd_{90}Si_{10}$	$12 \pm 5\%$	$23 \pm 6\%$
	$29 \pm 3\%$	$54 \pm 5\%$
	$33 \pm 2\%$	$63 \pm 3\%$

measurement was taken ($F_0 = E/S_0$). As a result, a two-dimensional map of the normalized fluence of the laser beam was obtained (see Fig. 3b). Normalization is essential because the contours were obtained from spots generated at different incidence pulse energies E. For any specific spot formed at a given incidence pulse energy E_s the normalized fluence map can be converted into an absolute fluence map by multiplying the normalized fluence by the corresponding maximum fluence F_s, defined as $F_s = F_{th}\exp(-S(E_s)/S_0)$, where $S(E_s)$ is the area enclosed by the iso-fluence contour.

The above-described procedure was employed to correlate the XRD measurements with the local fluence of the pump laser beam. SEM images acquired after XRD characterization were used for that purpose. These images revealed surface contamination by hydrocarbon residues in the vacuum chamber, induced by microfocused X-ray radiation during synchrotron measurements (see Fig. 3c). The visibly contaminated regions extend approximately 2–3 times beyond the nominal X-ray beam size due to the low-intensity tails of the X-ray beam. Normalized fluence maps were superimposed onto the SEM images for each investigated spot. Identifying the trace of each X-ray measurement point on these maps made it possible to correlate the atomic structure information obtained from XRD with the corresponding local irradiation fluence. Monitoring the XRD pattern as a function of the X-ray exposure time did not reveal any changes during data acquisition except for surface darkening induced by X-rays radiation.

3.2. XRD results

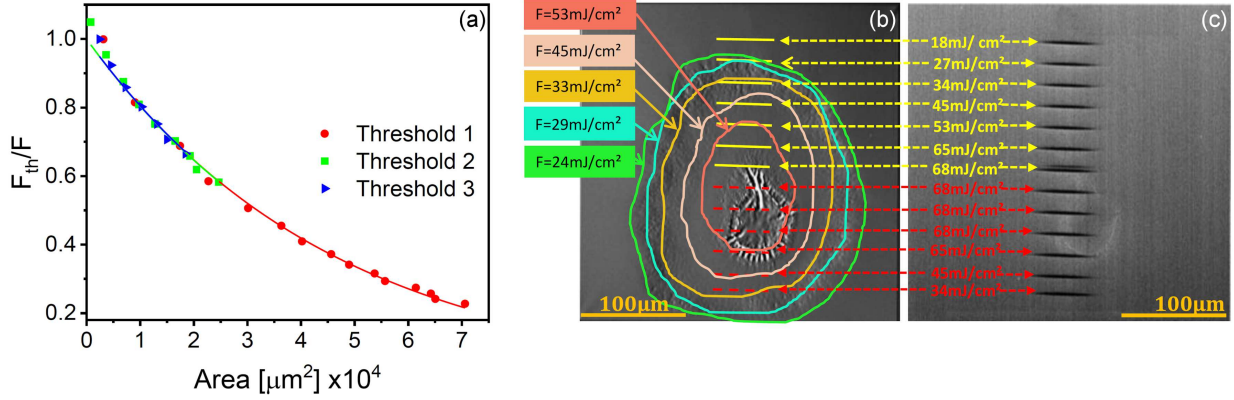The diffraction geometry was calibrated using an experimental 2D XRD pattern from a CeO_2

Fig. 3. (a) Inverse normalized fluence as a function of contour areas F_{th}/F vs S for all thresholds. (b) Optical microscopy and (c) SEM images of a laser-irradiated spot on a $Pd_{95}Si_{05}$ sample. The iso-fluence surface modification contours after laser irradiation are shown as color lines in (b). The positions of surface contamination caused by the X-ray micro-beam (black lines in (c)) are projected onto the optical microscopy image (b) as horizontal lines. The estimated fluences are assigned to each of the XRD measurement spots. In this work, only the spots marked with yellow color are investigated, as described in the text.

reference sample (SRM 674b) using the PyFAI software package [20]. XRD images of the as-grown and irradiated samples show continuous Debye–Scherrer rings (see example in Fig. 1b), indicating randomly oriented nanocrystallites in $Pd_{100-x}Si_x$ films. This enabled the 2D data to be reduced to 1D patterns through azimuthal integration (again using PyFAI). The XRD profile of a SiN membrane with only a SiN capping (total SiN thickness of about 55 nm) but without a $Pd_{100-x}Si_x$ film was used for the background subtraction for all 1D data before further analysis.

Figure 4 shows the background-subtracted 1D patterns for each sample irradiated at a local fluence level within the range 45–50 mJ/cm^2, i.e., between the 1st and 2nd threshold (panel (a)) and an example of the Rietveld analysis for the case of a $Pd_{95}Si_{05}$ sample laser-irradiated with a fluence of 45 mJ/cm^2 (panel (b)). Bragg diffraction peaks from the fcc-Pd phase (ICSD 77885) were identified for all samples except for $Pd_{83}Si_{17}$. In the latter case, only broad "halo" peaks were observed, indicating that the sample was in an amorphous state. This reflects a different structural response of the high-Si amorphous matrix to ultrafast heating and explains the differences in laser-irradiation-induced surface changes, as studied with optical microscopy (see Fig. 2e), compared to samples with lower Si content. The near-eutectic Pd–Si alloy is a good glass former even for relatively low cooling rates. Increasing the cooling rate (by applying ultrafast laser heating) further enhances its tendency to remain amorphous. Consequently, this sample was excluded from further crystallization analysis, and we focus on investigating the structural changes in the $Pd_{100-x}Si_x$ films ($x = 0, 3, 5, 10$ at.%). Instead, the XRD pattern obtained for the as-grown $Pd_{83}Si_{17}$ sample (which is also in an amorphous state) was

used as a reference amorphous signal to estimate the content of the amorphous phase in partially crystalline samples, as described below.

The XRD patterns collected across the modified area show a drastic decrease in the total signal intensity at the center of the irradiated spots, indicating partial material removal. In contrast, significantly increased Bragg peak intensities are observed in the surrounding rim and inner wrinkles region, which we attribute to local deposition of material from the center of the spot. Moreover, beyond the uniform Debye–Scherer rings — signifying randomly oriented nanocrystals — the distinct bright spots from this region appear in the 2D diffraction images, suggesting the existence of large crystallites. As a result, asymmetry and shoulders in the Bragg peak profiles of the integrated XRD patterns indicate the presence of the fcc phase of Pd with varying crystal size and lattice parameters at the same measurement location. Therefore, further analysis of structural changes in this study is limited to the first modified region, i.e., the region between the blue and purple contour lines in Fig. 2, where the surface area remains uniform and no significant changes or damage — apart from the formation of the outer wrinkles ring — are observed.

Rietveld refinement and size and strain analysis of the integrated XRD patterns were performed using Profex software [21]. To properly analyze the size and strain of the nanocrystallites in $Pd_{100-x}Si_x$ films, the instrumental profile was defined using the collected and integrated diffraction pattern of the CeO_2 reference material (SRM 674b). The instrumental effects were particularly taken into account using a "learning procedure" in the BGMN kernel of Profex [21]. This calibration considers the wavelength and optical divergence of the incident synchrotron beam, as well as the detector parallax

effect [22]. Figure 4b shows an example of the Rietveld refinement result for a $Pd_{95}Si_{05}$ sample laser-irradiated with a fluence of 45 mJ/cm² (the calculated profile of the crystalline phase is shown separately from the scaled reference amorphous signal).

The Rietveld method models the XRD signal (Bragg peaks) originating solely from a crystalline phase (Fig. 4b, pattern (3)). In order to achieve a good match between the calculated (pattern (3)) and experimental data (pattern (1)), it was necessary to account for an amorphous component in the samples, which contributes to the diffraction pattern. Since the contributions of the SiN cap and SiN membrane had already been removed in prior stages of data processing, the remaining discrepancy indicates the presence of an amorphous/highly disordered state of Pd alongside its crystalline phase. To account for this discrepancy, the azimuthally integrated pattern measured on the as-grown $Pd_{83}Si_{17}$ sample was used as a reference amorphous signal when refining the patterns obtained from all other $Pd_{100-x}Si_x$ samples using a function in Profex software [21]. The signal from the amorphous sample was scaled by a constant factor and shifted by a fixed value along the intensity axis (Fig. 4b, pattern (4)). Based on the scaling factor, the relative fraction of the amorphous phase contained in samples with different Si concentrations was estimated (see Fig. 5e).

When incorporating the amorphous phase into the Rietveld refinement using this approach, its intrinsic limitations should be considered. First, the shape of the diffuse scattering arising from thermal vibrations and structural defects closely resembles that of the amorphous phase, making it difficult to distinguish these contributions unambiguously. Second, the actual shape of the amorphous contribution may depend on the Si concentration. Thus, approximating the amorphous signal in all samples using a scaled $Pd_{83}Si_{17}$ diffraction pattern introduces some uncertainty into the refinement results. However, the atomic structure of eutectic metal–metalloid glasses, such as Pd–Si, can be envisioned as a dense random packing (DRP) of metal atoms, with smaller metalloid atoms occupying the canonical holes in the DRP structure [23]. This filling of holes leads to jamming of the packing and reduces the atomic mobility required for nucleation and growth of crystalline phases. In this picture, the metalloid atoms (in this case, Si) do not modify the skeleton with the DRP metal atoms (in this case, Pd) until all holes are filled (until ≈ 20 at.% Si is reached). Since the atomic number of Pd ($Z = 46$) is significantly higher than that of Si ($Z = 14$), the scattering contribution of Pd atoms is much higher than that of Si atoms in the XRD pattern. It thus follows that the XRD pattern of amorphous $Pd_{83}Si_{17}$ is a reasonable approximation also for the Si-poor Pd–Si amorphous structures. The high quality of the Rietveld fits, reflected by
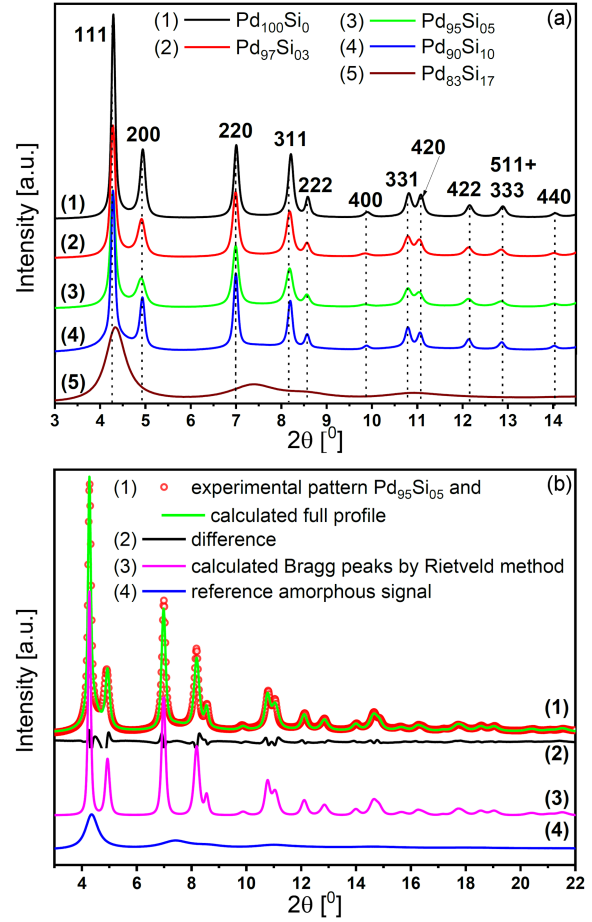

Fig. 4. (a) Integrated patterns for laser-irradiated Pd, $Pd_{97}Si_{03}$, $Pd_{95}Si_{05}$, and $Pd_{90}Si_{10}$ samples with fluences of 47, 50, 45, 48, and 49 mJ/cm², respectively. Bragg peaks from the crystalline Pd phase (ICSD 77885) are indexed. The $Pd_{83}Si_{17}$ sample is completely amorphous and only broad "halo" peaks are observed in both the as-grown (not shown) and annealed states. (b) Rietveld refinement for a laser-irradiated $Pd_{95}Si_{05}$ sample. Shown are the overlapped experimental and fitted XRD pattern (1), the difference (2), and the components of the fit (calculated pattern from crystalline part (3), and reference amorphous signal (4)). Rietveld refinement was performed in a 2θ angular range from 3 to 22°. Pattern (3) in panel (a) is a magnified view of experimental pattern (1) in panel (b), used to compared different samples with higher resolution to clearly mark the Bragg peaks and show differences between the samples.

the close agreement between the experimental and modeled patterns, further supports the reliability of our approach.

The thermal Debye–Waller factor, represented by the isotropic atomic displacement parameter B_{iso}, was fixed during the analysis. It was excluded from the refinement of the XRD patterns for all samples due to its strong correlation with other refined parameters, such as microstrain and crystallite size.
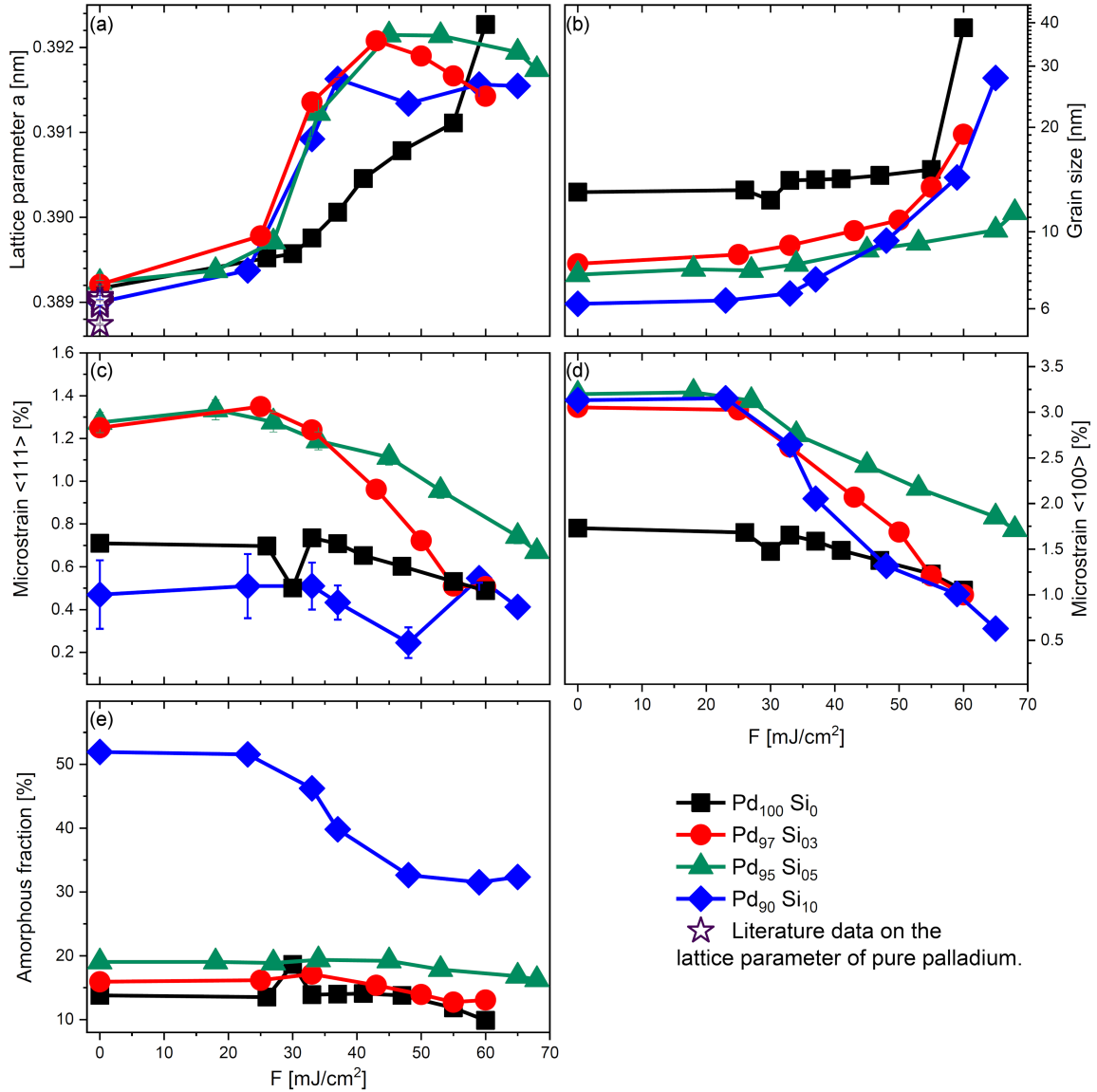
Fig. 5. Dependence of lattice parameters (a), grain sizes (b), microstrain (c, d) and amorphous phase fraction (e) on energy fluence. Error bars are marked with vertical lines, unless they are smaller than the size of the marker.

Simultaneous refinement of B_{iso} together with these parameters yielded unphysically low values in the range of 0.2–0.3 Å^2. For all refinements, a room-temperature value of $B_{iso} = 0.5$ Å^2 [24] was adopted.

The results of the Rietveld refinement are summarized in Fig. 5. The analysis revealed a dependency on the laser fluence for several structural parameters, including: lattice parameter (Fig. 5a); crystallite size (Fig. 5b); anisotropic microstrain, reflecting lattice parameter heterogeneity within crystallites (Fig. 5c and d); and the fraction of the amorphous phase (Fig. 5e).

The structural parameters for the as-grown samples are shown in Fig. 5 as data points at zero laser fluence. The lattice parameters for all as-grown samples are nearly identical and consistent with

values reported in the literature [24]. The main difference between samples with different compositions $x = 0, 3, 5, 10\%$ is the crystallites size, which was primarily measured in the in-plane direction of $Pd_{100-x}Si_x$ films due to the transmission diffraction geometry used. A clear trend is observed, in which the mean crystallite size decreases from ≈ 13 nm in pure Pd to about 6 nm in the $Pd_{90}Si_{10}$ sample — evidence of the influence of Si content on the grown process.

Anisotropic microstrain reflecting the heterogeneity in the lattice parameter within the crystallites was observed in all nanocrystalline samples prior to irradiation (Fig. 5c and d). Similar behavior was reported previously for nanocrystalline Pd [25–27]. In the pure Pd sample, the microstrain values were 1.7% along the crystallographic direction ⟨100⟩ and

0.7% along $\langle 111 \rangle$. For the $Pd_{100-x}Si_x$ samples containing 3% and 5% Si, a significant increase in microstrain was observed, reaching $\approx 3.1\%$ and 1.3% in the $\langle 100 \rangle$ and $\langle 111 \rangle$ directions, respectively. This increase may be attributed to the reduction in grain size and the presence of the Si alloy component, which introduce local distortions in the crystal lattice. Interestingly, the microstrain along the $\langle 111 \rangle$ direction in the $Pd_{90}Si_{10}$ sample is smaller than the one observed in pure Pd ($\approx 0.5\%$).

The amorphous phase content of the as-grown pure Pd sample was calculated from the reference amorphous signal scaling factor and was estimated to be 13%. This high apparent value includes contributions from thermal diffuse scattering at room temperature, which is considered as a part of the amorphous signal, as described above. Additionally, a highly defective regions with large disorder at grain boundaries may contribute to the observed amorphous features in the XRD patterns. In the $Pd_{97}Si_{03}$, $Pd_{95}Si_{05}$, and $Pd_{90}Si_{10}$ samples, the amorphous phase fraction increases to approximately 16%, 19%, and 52%, respectively (see Fig. 5e).

Correlation of the XRD measurements with the spatial fluence map allowed to analyze trends of structural changes as a function of local energy density. A slight increase of lattice parameters is observed at low fluences below 25 mJ/cm^2 (Fig. 5a). This can be explained by trapping the studied systems in an expanded state after the heating and cooling cycle. As the fluence increases above the threshold of 25 mJ/cm^2 up to ≈ 45 mJ/cm^2, the lattice parameters of the $Pd_{97}Si_{03}$, $Pd_{95}Si_{05}$ and $Pd_{90}Si_{10}$ samples increase from approximately 0.3895 ± 0.0005 nm to 0.3920 ± 0.0005 nm (Fig. 5a). At higher fluences, the lattice parameter becomes less sensitive to fluence changes and only a slightly decreasing trend is observed. In contrast, the lattice parameter of pure Pd continues to increase up to 60 mJ/cm^2, distinguishing its behavior from that of all the Si-containing alloys.

Changes in the lattice parameters in $Pd_{100-x}Si_x$ thin films are correlated with changes of the surface morphology observed by optical microscopy. A significant increase of lattice parameters is observed within the outer wrinkles ring, in the vicinity of the first fluence threshold of ≈ 25 mJ/cm^2 (Table II). We interpret this surface deformation as the result of a macroscopic lateral stress gradient caused by changes in the lattice parameter across the threshold. The lattice parameters of the as-grown samples (mostly measured in the in-plane direction) are close to literature data for powder bulk Pd. After laser annealing, the lattice parameter increases, indicating that Pd is subjected to expansive stress compared to the initial state. This stress could be thermally induced by the rapid heating–cooling cycle due to the difference in thermal expansion coefficients of the $Pd_{100-x}Si_x$ films and the SiN substrate.

The mean crystallite size in Pd, $Pd_{97}Si_{03}$ and $Pd_{95}Si_{05}$ samples increases moderately in the fluence range from 25 to 50 mJ/cm^2 (Fig. 5b). At higher fluences, which correspond to the fluences close to the second threshold (see Table II), a pronounced growth in the mean grain size is observed for Pd and $Pd_{97}Si_{03}$. In the $Pd_{90}Si_{10}$ sample, a noticeable increase in the mean grain size begins at higher fluence, above ≈ 35 mJ/cm^2. The extent of grain growth is more significant in the $Pd_{100-x}Si_x$ samples with higher Si content. These changes in crystallite size correlate with a reduction of the amorphous phase fraction (Fig. 5e), which is also more pronounced in samples with higher Si content. However, for sample $Pd_{90}Si_{10}$, an increase of the amorphous fraction is observed for fluences higher than 60 mJ/cm^2.

Microstrain in the Pd nanocrystallites decreases for all samples at fluences above 25 mJ/cm^2 (Fig. 5c and d). The trend of microstrain reduction closely follows the trend of increasing mean grain size.

4. Discussion

Irradiation of a metallic film with femtosecond laser pulses leads to its ultrafast heating, driven by energy transfer from photoexcited electrons to the ionic lattice via electron–phonon coupling occurring on a few picosecond timescale. Heating is followed by rapid cooling of the film via diffusion of the heat into the substrate occurring within a few nanoseconds [13], establishing a time frame for structural transformations. In our interpretation, given the sluggish kinetics in the solid state, any changes in grain size, microstrain or amorphous fraction in this time window require at least partial melting of the film. Here, we argue that atomic diffusion in solids is too slow to allow any considerable structural rearrangement during the very fast heating–cooling cycle, and only liquid state atomic diffusion, which is several orders of magnitude higher than in the solid phase, can account for our current observations. We note that a similar onset of ultrafast structural transformations coinciding with reaching the melting threshold was reported earlier for films irradiated with a femtosecond laser [28]. Based on the above arguments, the presumed melting threshold fluence is ≈ 25 mJ/cm^2. By taking into account the optical properties of Pd, we estimate the corresponding deposited energy density as 0.64 MJ/kg for the pure Pd sample. The obtained value is slightly higher than the melting threshold onset of ≈ 0.5 MJ/kg for thin pure Pd films reported in [15]. These estimations support the current interpretation of the experimental data.

According to the proposed scenario, melting is preferentially initiated in the already disordered grain-boundary regions [15, 29, 30]. Furthermore, partial melting predominantly affects small grains

due to the Gibbs–Thomson effect, and subsequent recrystallization on cooling leads to the formation of a coarser, less-strained microstructure. For all investigated samples, the heating–cooling cycle results in a decrease in the amorphous fraction. It is more pronounced in the case of high Si-content alloys, which is related to their initial structure. While the amorphous phase contribution is insignificant for the samples bearing up to 5% of silicon, in the as-deposited $Pd_{90}Si_{10}$ film it exceeds 50%. This observation is consistent with an increasing glass-forming ability for a Si content approaching the eutectic composition.

An important observation is that the formation of crystalline Pd–Si intermetallic phases was not observed in each of the samples. According to the equilibrium phase diagram of the Pd–Si system [4, 6], several Pd–Si compounds should form for the investigated compositions, especially $Pd_{21}Si_5$. However, across all samples and irradiation conditions, only the fcc-Pd crystalline phase was observed. In our interpretation, the phase selection occurring both during thin-film deposition and during subsequent ultrashort-pulsed laser annealing is governed primarily by kinetic constraints rather than thermodynamic stability. Because the system experiences extremely rapid quenching from high-temperature regime, where atomic mobility would normally allow for the nucleation and growth of the equilibrium phases, Pd–Si intermetallic compounds do not have sufficient time to form. Instead, the system is trapped in a metastable configuration, leading to the formation of an fcc Pd(Si) solid solution rather than the thermodynamically stable Pd–Si compounds.

5. Conclusions

The combined use of microscopy and XRD provided new insights into the composition-dependent crystallization behavior of $Pd_{100-x}Si_x$ thin films. By analyzing optical images from a series of laser irradiations at varying pulse energies (fluence scan), a two-dimensional fluence map was reconstructed for an arbitrary pulse energy. This enabled a direct correlation between deposited energy density, surface morphology, and structural changes derived from XRD measurements analyzed using the Rietveld method. Below the threshold of ≈ 25 mJ/cm^2, laser irradiation induces minimal changes, aside for a slight lattice expansion due to ultrafast heating–cooling cycle. Above this threshold, all samples exhibit significant structural modifications: strain reduction, grain growth, and diminished amorphous contributions. These observations are consistent with the picture in which the sample, upon ultrafast laser annealing, undergoes a relaxation towards lower energy state. Since the relaxation occurs on a nanosecond time scale, too short for significant structural rearrangement in the solid state, it is reasonable to assume that the laser-irradiated films undergo (partial) melting. This melting, preferentially initiated in the disordered grain-boundary regions and predominantly affecting small grains, is followed by rapid recrystallization into a coarser, less-strained microstructure. Notably, only fcc-Pd crystalline phase was observed across all samples and irradiation condition, in contrast to the equilibrium phase diagram including the Pd–Si compounds. It confirms that the fast, non-equilibrium processes involved in the sample deposition and laser treatment lead to the formation of metastable states.

References

[1] A. Inoue, N. Nishiyama, T. Matsuda, *Mater Trans JIM* **37**, 181 (1996).

[2] K. Georgarakis, D.V. Louzguine-Luzgin, J. Antonowicz, G. Vaughan, A.R. Yavari, T. Egami, A. Inoue, *Acta Mater* **59**, 708 (2011).

[3] B. Sarac, A.S. Sarac, J. Eckert, *J. Electrochem. Soc.* **170**, 014503 (2023).

[4] D.V. Louzguine-Luzgin, K. Georgarakis, V. Zadorozhnyy, N. Chen, K. Nakayama, G. Vaughan, A.R. Yavari, A. Inoue, *Intermetallics* **20**, 135 (2012).

[5] I. Rodríguez, R.M. Valladares, A. Valladares, D. Hinojosa-Romero, A.A. Valladares, *Sci. Rep.* **12**, 4624 (2022).

[6] H. Okamoto, *J. Phase Equilibria* **14**, 536 (1993).

[7] K. Yao, N. Chen, *Sci. China Ser G Physics, Mech Astron* **51**, 414 (2008).

[8] L. Zhong, J. Wang, H. Sheng, Z. Zhang, S.X. Mao, *Nature* **512**, 177 (2014).

[9] Z.J. Yang, L. Tang, T.Q. Wen, KM. Ho, C.Z. Wang, *J. Phys. Condens. Matter.* **31**, 135701 (2019).

[10] M. Celtek, S. Sengul, U. Domekeli, V. Guder, *J. Mol. Liq.* **372**, 121163 (2023).

[11] M. Von Allmen, S.S. Lau, M. Mäenpää, B.Y. Tsaur, *Appl. Phys. Lett.* **36**, 205 (1980).

[12] C-J. Lin, F. Spaepen, D. Turnbull, *J. Non. Cryst. Solids* **61**–**62**, 767 (1984).

[13] J. Antonowicz, P. Zalden, K. Sokolowski-Tinten et al., *J. Alloys Compd.* **887**, 161437 (2021).

[14] A.P. Radliński, A. Calka, B. Luther-Davies, *Phys. Rev. Lett.* **57**, 3081 (1986).

[15] J. Antonowicz, A. Olczak, K. Sokolowski-Tinten et al., *Acta Mater.* **276**, 120043 (2024).

[16] L. Silson, P. Insight, Warwickshire CV47 1NE England.

[17] N. Schell, A. King, F. Beckmann, T. Fischer, M. Müller, A. Schreyer, *Mater. Sci. Forum* **772**, 57 (2013).

[18] J. Chalupský, T. Burian, V. Hájková, L. Juha, T. Polcar, J. Gaudin, M. Nagasono, R. Sobierajski, M. Yabashi, J. Krzywinski, *Opt Express* **21**, 26363 (2013).

[19] J.M. Liu, *Opt. Lett.* **7**, 196 (1982).

[20] G. Ashiotis, A. Deschildre, Z. Nawaz, J.P. Wright, D. Karkoulis, F.E. Picca, J Kieffer, *J. Appl. Crystallogr.* **48**, 510 (2015).

[21] N. Doebelin, R. Kleeberg, *J. Appl. Crystallogr.* **48**, 1573 (2015).

[22] F. Marlton, O. Ivashko, M.V. Zimmerman, O. Gutowski, A.C. Dippel, M.R.V Jørgensen, *J. Appl. Crystallogr.* **52**, 1072 (2019).

[23] C. Bennett, D. Polk, D. Turnbull, *Acta Metall.* **19**, 1295 (1971).

[24] J.A. Eastman, M.R. Fitzsimmons, L.J. Thompson, *Philos. Mag. B* **66**, 667 (1992).

[25] Y. Oba, T. Sato, T. Shinohara, *Phys. Rev. B* **78**, 224417 (2008).

[26] K. Reimann, R. Würschum, *J. Appl. Phys.* **81**, 7186 (1997).

[27] A. Stukowski, J. Markmann, J. Weissmüller, K. Albe, *Acta Mater.* **57**, 1648 (2009).

[28] A.R. Khorsand, R. Sobierajski, E. Louis et al., *Opt. Express* **18**, 700 (2010).

[29] A.F. Suzana, R. Koch, L. Wu et al., *Phys. Rev. B* **107**, 214303 (2023).

[30] T.A. Assefa, Y. Cao, S. Banerjee et al., *Sci. Adv.* **6**, 1 (2020).